JGR Atmospheres

RESEARCH ARTICLE
10.1029/2023JD040535

Meteorological Drivers of North American Monsoon Extreme Precipitation Events

Shiheng Duan[1], **Paul Ullrich**[1], **and William R. Boos**[2]

[1]Atmospheric Science Graduate Group, University of California, Davis, Davis, CA, USA, [2]Department of Earth and Planetary Science, University of California, Berkeley, Berkeley, CA, USA

Key Points:

- Seven subregions of the North American Monsoon with distinct precipitation characters are identified
- Gulf of California moisture surges, mesoscale convective systems and frontal systems are primary drivers of extreme precipitation
- A probability analysis reveals the nonlinear and non-additive characters of the interactions among extreme precipitation event drivers

Supporting Information:

Supporting Information may be found in the online version of this article.

Correspondence to:

S. Duan,
shiduan@ucdavis.edu

Citation:

Duan, S., Ullrich, P., & Boos, W. R. (2024). Meteorological drivers of North American monsoon extreme precipitation events. *Journal of Geophysical Research: Atmospheres*, *129*, e2023JD040535. https://doi.org/10.1029/2023JD040535

Received 21 DEC 2023
Accepted 18 JUN 2024

Abstract In this paper the meteorological drivers of North American Monsoon (NAM) extreme precipitation events (EPEs) are identified and analyzed. First, the NAM area and its subregions are distinguished using self-organizing maps applied to the Climate Prediction Center global precipitation data set. This reveals distinct subregions, shaped by the inhomogeneous geographic features of the NAM area, with distinct extreme precipitation character and drivers. Next, defining EPEs as days when subregion-mean precipitation exceeds the 95th percentile of rainy days, five synoptic features and one mesoscale feature are investigated as potential drivers of EPEs. Essentially all EPEs can be associated with at least one selected driver, with only one event remaining unclassified. This analysis shows the dominant role of Gulf of California moisture surges, mesoscale convective systems and frontal systems in generating NAM extreme precipitation. Finally, a frequency and probability analysis is conducted to contrast precipitation distributions conditioned on the associated meteorological drivers. The findings demonstrate that the co-occurrence of multiple features does not necessarily enhance the EPE probability.

Plain Language Summary Extreme precipitation is of great importance for both geophysical and socioeconomic reasons. This study first identifies geographic subregions of the North American Monsoon within which extreme precipitation exhibits distinct characteristics. The extreme precipitation events in each subregion are then associated with at least one candidate atmospheric driver, revealing the dominant precipitation drivers among subregions. Depending on the subregions and driver, precipitation rates may increase or decrease when two candidate factors co-occur. Several such double driver combinations are examined.

1. Introduction

Monsoons are continental-scale circulation systems that develop in response to seasonal changes in the contrast in energy sources between continents and adjacent oceanic regions (Geen et al., 2020; Vera et al., 2006). They are known for driving substantial regional precipitation, and are critical to the Earth's hydroclimate system. In this study, we focus on the North American Monsoon (NAM) and examine the meteorological environments and feature drivers of both precipitation and extreme precipitation when the NAM is active. We show that essentially all extreme precipitation events (EPEs) can be linked to one or more meteorological features. This feature-based decomposition is subsequently employed to draw novel insights into the drivers of precipitation in the NAM and its subregions.

The first challenge in characterizing precipitation in the NAM is to actually delineate the NAM region. The NAM differs from other monsoon regions as it does not exhibit the typical seasonal zonal wind reversal (de Carvalho & Jones, 2016), which is frequently used to define monsoon indices for other regions (Goswami et al., 1999; Hung & Yanai, 2004; B. Wang & Fan, 1999; Webster & Yang, 1992). Precipitation seasonal variability is alternatively used to identify monsoonal regions (Liu et al., 2016), and under this metric, the NAM region refers to the region roughly bounded to the south by Central America and stretching into the southwestern US (Lee & Wang, 2014; Liu et al., 2016; Mohtadi et al., 2016; B. Wang et al., 2018). The NAM Experiment (NAME, W. Higgins et al., 2006) offers a localized definition of the NAM region, which roughly encompasses the southwestern United States and northwestern Mexico (Figure 1, dashed red polygon). This region is much smaller and offset to the north from the NAM region that emerges from precipitation seasonal variability (e.g., B. Wang et al., 2018). Others have used "NAM region" to refer to a rectangular latitude-longitude box, or to specific states such as Arizona or New Mexico (Cook & Seager, 2013; Douglas & Englehart, 2007; Finch & Johnson, 2010; Varuolo-

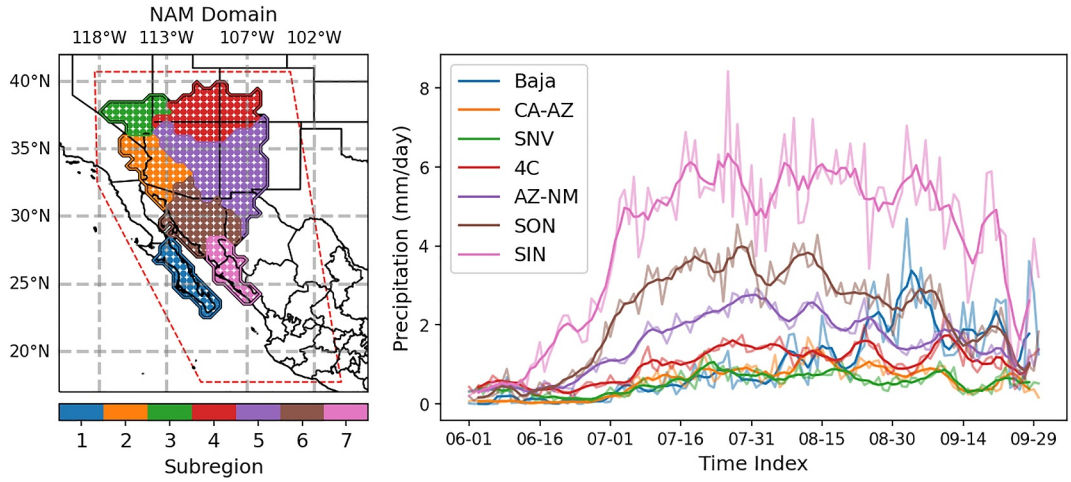

Figure 1. The North American Monsoon (NAM) regional domain. The dashed red contour on the left is adapted from the NAM Experiment Forecast Forum. The filled shapes denote the domain and subdomains identified from the ensemble Self organizing maps in this study, with dots inherited from the 0.5° Climate Prediction Center precipitation data set. The thin lines in the right panel represent the long-term daily mean precipitation. For easier visualization, a 5-day mean smoothing is performed to obtain the thick line.

Clarke et al., 2019). Although these choices can simplify computations, such approximations may not be appropriate for regional precipitation studies. Such structured regions may cover areas with dissimilar precipitation mechanisms and drivers. This is especially true in the vicinity of the NAM, where the complex terrain leads to precipitation being shaped by the mechanical influence of orography on winds, together with local thermodynamic conditions (Boos & Pascale, 2021). As such, we argue that a delineation of the NAM region emphasizing local precipitation features should be used for studies focused on NAM precipitation. Identification of the "NAM region" in this manner, along with subregions which we will discuss later, is necessary to establish a foundation for the precipitation and extreme precipitation analysis pursued in this study.

EPEs, which occur when the precipitation rate is in the long tail of its distribution, are generally defined as events where the precipitation rate exceeds a certain threshold, typically using one of two methods: parametric or non-parametric (Anagnostopoulou & Tolika, 2012). The parametric approach involves parameter estimation of the precipitation distribution (Acero et al., 2011; Alaya et al., 2020), whereas the non-parametric approach often adopts percentiles, such as the 95th or 99th percentile precipitation rate of rainy days (pq95 or pq99, Agel et al., 2018; Kunkel et al., 2012; Myhre et al., 2019). In this study, we adopt the non-parametric approach and define the threshold for EPEs as pq95.

To understand the meteorological causes of EPEs, previous studies have examined potential meteorological features (Barlow et al., 2019; Kunkel et al., 2012). Specific to the NAM region, Díaz et al. (2008) and Englehart and Douglas (2001) identified tropical cyclones (TCs) as the primary feature affecting precipitation in Baja California. In Bordoni and Stevens (2006) and Johnson and Delworth (2023), the role of Gulf of California (GOC) moisture surges was highlighted. These events boost continental humidity, provide the water vapor necessary for precipitation, and decrease the moist convective stability of the environment. Moisture surges' impact on precipitation was also studied in F. Dominguez et al. (2016), where numerical simulations demonstrated that advected moisture from the GOC was the greatest contributor to non-locally-sourced precipitation in the NAM region. Frontal systems were found to be another significant driver associated with 44% of EPEs in the southwestern US summertime, as shown in Kunkel et al. (2012). In addition to near-surface features, upper-level disturbances were identified as influential controls on precipitation by Igel et al. (2021), who examined the impact of tropical upper troposphere troughs (TUTTs) on NAM precipitation, and Sierks et al. (2020), who highlighted the role of Rossby wave breaking (RWBs) and inverted troughs (ITs) over Lake Mead. Beyond these synoptic features, Finch and Johnson (2010) and Mejia et al. (2016) revealed the significance of mesoscale convection system (MCS) activities in the NAM region. These previous studies provide candidate meteorological systems to comprehensively understand the drivers of NAM precipitation.

In this study, our primary objective is to conduct a comprehensive analysis of the NAM EPE drivers, their associated precipitation, and interactions among these drivers. The NAM domain and its subregions are first identified from a gridded precipitation data set, with regions delineated using local precipitation characteristics. The drivers of precipitation and EPEs in these regions are subsequently investigated using feature tracking and attribution. Section 2 describes the precipitation and reanalysis data sets in this study. The precipitation-based NAM domain and subdomain demarcation is described in Section 3. Section 4 introduces the candidate drivers of the NAM EPEs, as well as the corresponding detection methods and data sets, then examines the distribution of precipitation related to each driver.

2. Data

In this study, precipitation data from the Climate Prediction Center (CPC) Global Unified Gauge-Based Analysis of Daily Precipitation (referenced to as the CPC data set) is used. CPC data is based on gauge observations and provides daily precipitation analysis globally at 0.5° grid spacing from 1 January 1979 to present (Xie et al., 2010). Since the CPC data set relies on gauge observations, the specific time period that defines a day varies across the globe. For CONUS and Mexico, they share the same time window: from 12Z to 12Z. Meteorological conditions are derived from the ERA5 reanalysis data set. This product provides hourly reanalysis atmospheric fields with a 30-km horizontal resolution (Hersbach et al., 2020). The record spans from 1950 to present, although we subset the period 1979 to 2018 to coincide with the meteorological driver data sets coverage. Additionally, when the hourly data is averaged to derive daily records, the time window is set to 12Z–12Z to accord with the CPC precipitation time interval.

3. Identification of NAM Subregions

3.1. Self Organizing Maps

Self organizing maps (SOMs) is an unsupervised machine learning method that takes high-dimensional data as input and creates spatially organized internal representations of input vectors (Kohonen & Honkela, 2007). Details on the training process can be found in Kohonen and Honkela (2007). After the SOMs has converged, each sample is assigned to a node, which can be viewed as the cluster label.

SOMs has been applied in previous studies for atmospheric pattern recognition. For example, Agel et al. (2018) used SOMs with tropopause pressure anomalies to find the large-scale patterns associated with extreme precipitation. In this work we follow Swenson and Grotjahn (2019), who used SOMs to classify different precipitation regimes over the CONUS. Before applying SOMs, we first take the cube root of precipitation as in Stidd (1953) to transform it from a highly skewed distribution to an approximately normal distribution. Then the long-term daily mean (LTDM) is calculated following Equation 1, where $P_{i,n}$ represents the precipitation on the ith day in year n, and N is the total number of years in the record. The resulting LTDM, which spans 365 days, excluding leap days, is normalized to the range 0–1 before training the SOMs according to Equation 2. This normalization informs us of the occurrence of extreme precipitation normalized within each grid cell, rather than the absolute precipitation amount (Swenson & Grotjahn, 2019).

$$\mathrm{LTDM}_i = \frac{1}{N}\sum_{n=1}^{N} P_{i,n} \tag{1}$$

$$\mathrm{LTDM}_{\mathrm{normalized}} = \frac{\mathrm{LTDM} - \min(\mathrm{LTDM})}{\max(\mathrm{LTDM}) - \min(\mathrm{LTDM})}. \tag{2}$$

The number of output nodes (i.e., the number of clusters) is prescribed before training SOMs. Since there is no prior knowledge of the correct number of clusters, to avoid arbitrariness and ensure robustness, an ensemble method is employed with the number of nodes ranging from 10 to 20. The final NAM region is then based on the intersection of the total ensemble.

3.2. NAM Domain and Subregions

The SOM ensemble is first generated for the North America domain encompassing CONUS and Mexico. Results for this large domain are available in the supporting data set and selected results are depicted in Figure S1 in

Supporting Information S1. The ensemble intersection is similar but more compact when compared with the NAME domain, as shown in Figure 1. Figure S2 in Supporting Information S1 displays the ensemble result with a focus on the smaller regions near the NAM domain. Although the cluster boundaries vary with the number of clusters, the general locations and patterns are consistent among all the SOMs results. It should be noted that the SOMs approach does not ensure geographical continuity, so some minor manual tuning is performed to combine isolated grid points with neighboring regions. The boundaries we eventually identify for the NAM region are similar to those which emerge in the US Southwest from the work of Swenson and Grotjahn (2019, Figure 7), and cover all of Arizona and part of California, Nevada, Utah, Colorado and New Mexico. The differences in the western and northern boundaries (compared to their results) are attributed to sensitivity of the method to the addition of grid points outside of the CONUS.

Although the overall NAM domain emerges naturally from this SOMs analysis, further delineation of precipitation subregions is still necessary given the domain's heterogeneous geographical and topographical characteristics. The same SOMs-based approach is again applied to the identified NAM region, but instead of the all-year LTDM, only the summertime precipitation (June, July, August, and September) is used as input. The number of subregions is set to range from 2 to 10, and the metrics in Zhuang et al. (2020) are employed to assess the SOM performance. These metrics include mean correlation coefficient, quantization error, and maximum correlation between two nodes. A figure showing the metrics with respect to the number of subregions is presented in Figure S3 in Supporting Information S1. Increasing the subregion number leads to a reduction in quantization error, indicating greater distinction among data samples. Simultaneously, the correlation coefficient increases, suggesting greater similarity among nodes and introducing redundancy. Previous studies typically rely on predefined thresholds to determine the number of SOM nodes (e.g., Fettweis et al., 2011; Huang et al., 2017; Lund, 1963), based on their expertise. However, this practice may be subjective and need adaptation when applied to different variables. In this study, to balance accuracy and computational efficiency, the subregion number is determined by assessing the marginal effect of increasing the number of SOM nodes. Consequently, seven subregions are selected based on the relatively minor marginal changes in correlation and quantization error. It is important to note that varying the number of subregions can yield different outcomes. Nevertheless, a comprehensive examination of the sensitivity to the number of subregions falls beyond the scope of this study.

The selected seven subregions are depicted in Figure 1, along with their LTDM precipitation during summer. Subregions 1 through 7, respectively, refer to: (a) the southern half of the Baja California Peninsula (Baja); (b) Southeastern California, Northern Sonora and Eastern Arizona (CA-AZ); (c) southwestern Utah and most of southern Nevada (SNV); (d) the Colorado Plateau and the "Four Corners" region (4C); (e) most of the Arizona desert, New Mexico and Northern Chihuahua (AZ-NM); (f) most of Sonora (SON); and (g) Southern Sonora and Northern Sinaloa (SIN). Comparing the LTDM precipitation signal in each region, it is clear that coastal areas such as SIN and SON are wetter regions, with higher overall precipitation rates, while the inland deserts are relatively drier (e.g., CA-AZ and SNV). It is also clear that the timing of the shift to the wetter monsoonal precipitation regime varies by subregion. Throughout the literature, the precise definition of monsoon onset date varies: it is defined as the first day after 1 June when precipitation rate exceeds 0.5 mm/day and lasts for 3 days in R. Higgins et al. (1997), while the threshold is 1 mm/day and 5 consecutive days in Turrent and Cavazos (2009). This difference is primarily due to the area of interest: Turrent and Cavazos (2009) examined the whole NAM area, whereas R. Higgins et al. (1997) focused on New Mexico and Arizona, where the climatological precipitation signal is weaker. We adopt 1 mm/day and 5 days here, yielding the following median monsoon onset dates: 30 August for Baja, 30 July for CA-AZ, 20 July for SNV, 19 July for 4C, 6 July for AZ-NM, 4 July for SON and 30 June for SIN, respectively. The onset dates are generally earlier for more southern subregions, with Baja being a clear exception.

4. Synoptic and Mesoscale Features as Drivers for EPEs

4.1. EPE Definition

Herein, EPEs are defined as days when the daily subregion-mean precipitation rate exceeds the 95th percentile of rainy days (i.e., days with precipitation accumulation larger than 1 mm). When consecutive days exceed this threshold, sequential days are consolidated into a single event. As shown in Table 1, the EPE threshold varies across subregions. What stands out from Table 1 is the long tail of the distribution, evidenced by the fact that the median is less than the mean and the 95th percentile is several times larger than either in this zero-bounded

Table 1
Mean, Median, and 95th Percentile Precipitation in mm/day

	Baja	CA-AZ	SNV	4C	AZ-NM	SON	SIN
Mean	5.99	2.99	2.93	2.70	2.87	4.10	6.41
Median	3.21	2.11	2.07	2.08	2.33	2.98	4.55
95th percentile	21.36	7.98	7.63	6.30	6.47	10.65	17.25

distribution. This is especially true for Baja; its EPE threshold is higher than that of SIN, while SIN is wetter overall, with higher mean and median precipitation rates during rainy days. Additionally, the LTDM precipitation rate is higher in SON and SIN than in Baja, as shown in Figure 1, yet the EPE threshold is much higher in Baja. These differences highlight the discrepancy between precipitation climatology in the mean and the tail, and support the need for subregion delineation.

The number of EPEs in each subregion from 1979 to 2018 is available in Supporting Information S1 (Figure S4 in Supporting Information S1). Since the coastal regions have more rainy days, following our criteria, they also tend to have more EPEs. A Mann-Kendall (MK) test is applied to each subregion to see if there is a historical trend from 1979 to 2018 in the number of EPE events, EPE precipitation amount, and yearly EPE precipitation rate. Note that EPE precipitation rate is defined here as the EPE precipitation amount divided by the number of extreme precipitation days, which is not the same as the number of EPE events when there are consecutive extreme precipitation days. In most subregions, there are no significant trends at the 5% confidence level, however, EPE event numbers and precipitation amount do exhibit a significant increase in Baja and SON. Baja also shows a rising trend in EPE precipitation rate, while CA-AZ shows a declining trend. These changes are likely influenced by a combination of low-frequency climate variability and climate change (Cavazos et al., 2008; W. Zhang & Zhou, 2019). Despite the slight increasing trend in EPE precipitation for Baja and SON, the total precipitation on rainy days does not exhibit a statistically significant trend in either case. Thus, the increase in EPE precipitation in these regions are not accompanied by significant changes in the yearly total precipitation.

4.2. Selected Meteorological Features

In this work we focus on five synoptic features and one mesoscale feature: TCs, GOC moisture surges, upper tropospheric troughs (UTTs), frontal systems, mid-tropospheric lows, and MCS. These features are selected based on previous studies connecting them with EPEs (e.g., Barlow et al., 2019; Catto et al., 2012; Kunkel et al., 2012; Sierks et al., 2020). The following subsections introduce data sets for each feature and the procedure used to link these events with EPEs.

4.2.1. Tropical Cyclones

TC tracks from the International Best Track Archive for Climate Stewardship (IBTrACS) are used in this study (Knapp et al., 2010, 2018). IBTrACS provides 3-hourly records of TC locations and intensities around the world from 1842 to present (Knapp et al., 2010). We exclude tropical depressions from this analysis, selecting only tropical storms and hurricanes. A TC is linked to an EPE if its track is within a 5° radius of the given NAM subregion during the EPE period. This distance criterion is based on the general horizontal scale of TCs (C. Dominguez & Magaña, 2018; Jiang & Zipser, 2010; Kunkel et al., 2012).

4.2.2. Gulf of California Moisture Surges

GOC moisture surges are identified using ERA5 6-hourly reanalysis data by computing the vertical integral of vapor flux (IVT) from 1,000 to 300 hPa:

$$\mathrm{IVT} = -\frac{1}{g}\int_{1,000}^{300} qV\,dp \tag{3}$$

where g is gravity, q is specific humidity and V stands for velocity. Figure 2 shows the GOC transect with grid points aligned along the gulf in a 25-km spatial resolution. The northward and eastward IVT are used to obtain fluxes parallel to (IVT-A) and perpendicular to (IVT-B) the GOC transect, and the grid points along the perpendicular axis are averaged to derive a one-dimensional flux profile along the Gulf. Surge candidates are defined as fluxes that surpass the 95th percentile of vapor flux at each grid point. Spatio-temporally consecutive candidate grid points are then characterized as a surge event, which must last at least 12 hr. An illustration of this detection method is provided in Supporting Information S1 (Figure S5 in Supporting Information S1).

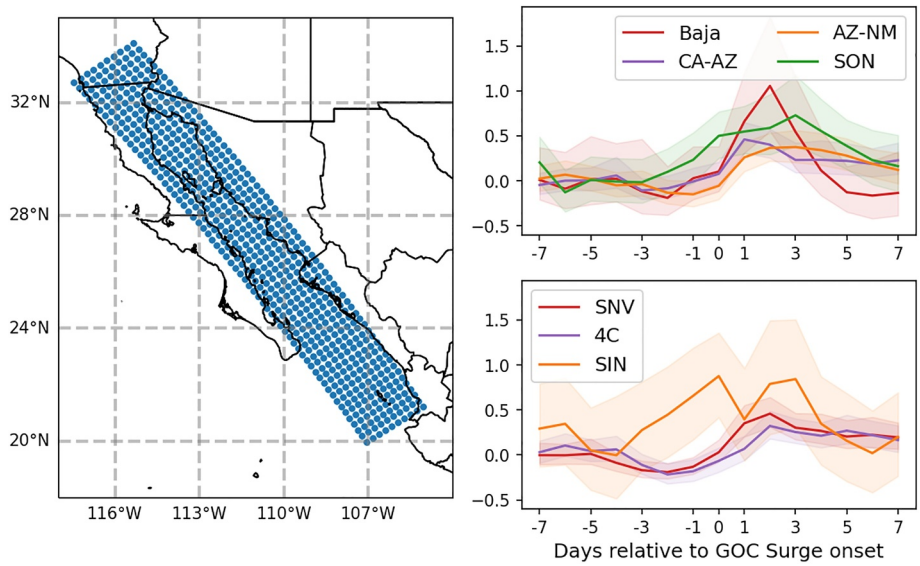

Figure 2. Gulf of California (GOC) transect grid point spacing (left) and precipitation anomaly composites of GOC Surges in mm/day (right). Shading indicates the 95% confidence intervals, generated by bootstrapping.

Figure 2 shows the precipitation anomalies with respect to the surge occurrence. The *x*-axis denotes days after the onset of surges with negative values representing days before the surge and positive for days after the surge. Most subregions show precipitation peaks 2 or 3 days after the onset date while SIN shows double peaks, albeit within a large uncertainty envelope, with the first peak on the onset date. In addition, the precipitation anomaly is negative one to 2 days before the onset date in SNV, 4C, and AZ-NM, suggesting dry conditions prior to surge arrival. An EPE is deemed to be driven by a GOC surge if a surge occurs within a specific time window before the EPE. The window size is set to 0 days for SIN, 1 day for CA-AZ, 2 days for Baja, SNV, 4C, and AZ-NM, and 3 days for SON.

4.2.3. Upper Tropospheric Troughs

The wide variety of upper-level disturbances (RWBs, Potential Vorticity [PV] streamers, TUTTs, ITs) all exhibit a local high in PV near the tropopause, commonly approximated by the 200 hPa level. In this study, all these upper-level features, referred to collectively as UTTs, are first identified as closed PV contours of value 2×10^{-6} m^2 s^{-1} K kg^{-1}, or 2 potential vorticity unit (PVU), from the ERA5 6-hourly 200 hPa PV using TempestExtremes (Ullrich et al., 2021). A filter is applied on prospective UTT candidates to remove coincident TCs, to ensure that only upper-level disturbances are extracted.

To better examine the effect of UTTs on regional precipitation, we composite precipitation anomalies (i.e., precipitation minus its LTDM) within a 20° radius of each tracked UTT in Figure 3. The radius of 20° is large enough to capture possible longer-range UTT impacts on precipitation. Only anomalies that satisfy a 95% confidence interval derived with a two-sided Student's *t*-test are plotted. Precipitation is consistently depressed to the north and northeast of the UTT center, and enhanced to the south and southeast. The enhancement reaches its peak and diminishes with distance within 10°. UTTs include both mid-latitude disturbances (RWBs) and tropical features (i.e., TUTTs). To examine these two types of UTTs, we separate the UTTs by their direction of propagation, and compose feature-centered precipitation in Figure 3, along with geographically-fixed PV200 and U200 for eastward and westward propagating UTTs. An illustration for SON is depicted in Figure S6 in Supporting Information S1, which suggests the propagation direction of the upper-level disturbances is generally determined by the large-scale background flow. Consequently, northern NAM subregions with frequent extratropical westerlies tend to experience more eastward-UTT related EPEs, as shown in Table 2.

Westward- and eastward-moving UTTs lead to very different precipitation anomalies, as depicted in Figure 3. Eastward UTTs exhibit enhanced precipitation to the southeast of the feature and suppressed precipitation in most of the other quadrants. On the other hand, the westward UTTs exhibit scattered and weak enhancement of

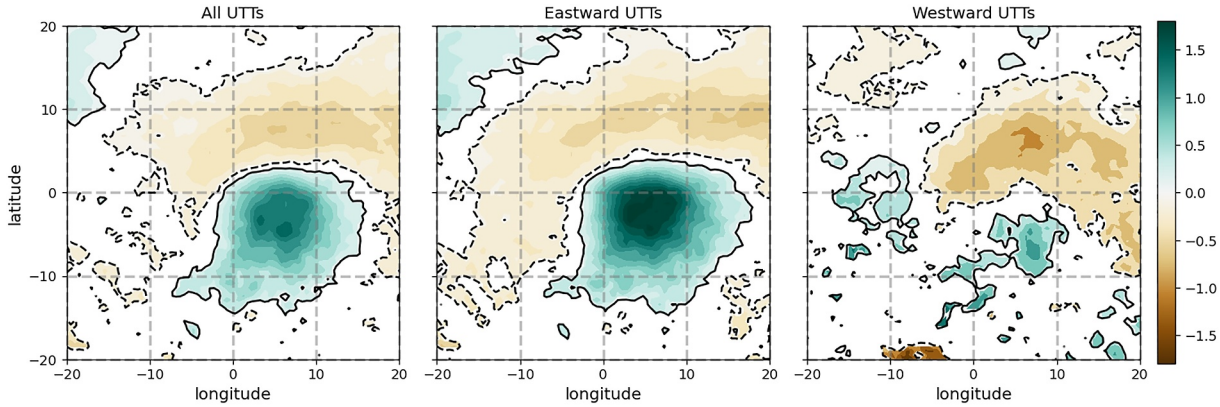

Figure 3. UTT-centered composites of precipitation anomalies with confidence level at 95%. Origin point represents the UTT centers. Colors show the precipitation anomaly in mm/day. Solid and dash lines are for confidence interval contours.

precipitation to the south and stronger suppression of precipitation to the northeast. This disparity in precipitation composites is further discussed in the following sections. Despite these differences in behavior, the precipitation enhancement is still within 10° of the UTT center for westward UTTs and so 10° is set as the criterion for UTTs. That is, if there is a concurrent UTT in the 10° radius from the subregion during the occurrence of an EPE, the EPE will be assigned to this UTT.

4.2.4. Frontal Systems

Despite the existence of automated identification methods for frontal systems, available schemes are insufficiently validated over the NAM region (Biard & Kunkel, 2019; Parfitt et al., 2017). Instead of identifying fronts from reanalysis data, a manually labeled data set from National Weather Service (NWS) coded surface bulletins is used. This NWS data set spans from 2003 to 2018 and provides the locations and types of frontal systems at 3-hr intervals, which are determined by a NWS meteorologist (Biard, 2019). To link EPEs with frontal systems, we use the method from Catto et al. (2012): If a concurrent front is 5° or less away from the EPE area, the EPE is associated with that front.

4.2.5. Mid-Tropospheric Lows

In addition to the surface-level and upper-level features, mid-tropospheric disturbances also play a big role in driving precipitation (Houssos et al., 2008; Wibig, 1999). In this study, we detect anomalous lows at the 500 hPa level and assess their importance as a driver of EPEs. The composite mean of 500 hPa geopotential anomaly during EPEs is shown in Figure 4. The low centers are generally located to the west of the inland subregions, and directly above the coastal subregions with weaker amplitudes, though all features are significant at the 95% confidence level. Given that compositing all EPEs may potentially attenuate the geopotential anomaly field, a strict threshold is set to isolate instances characterized by pronounced mid-tropospheric low conditions: where a concurrent Φ500 anomaly low stronger than $-1{,}000\ m^2/s^2$ is less than 5° away from the subregion, the EPE is associated with a mid-tropospheric low.

4.2.6. Mesoscale Convective Systems

MCSs are difficult to resolve in modern reanalysis data due to their small horizontal scale. Nonetheless, a variety of observational products possess sufficiently high resolution to enable MCS detection. Feng et al. (2021) tracked MCSs globally based on infrared brightness temperature and precipitation from satellite data sets from 2001 onward. In this study we analyzed a subset of this tracking data covering the NAM region. A MCS event is deemed to be associated with an EPE only if there are labeled MCS grid points inside the precipitating area.

Table 2
Number of UTT-EPE Events by Propagation Direction in Each Subregion

	Baja	CA-AZ	SNV	4C	AZ-NM	SON	SIN
UTT events	10	15	12	33	51	46	53
Westward	6	9	2	8	21	36	35
Eastward	4	6	10	25	30	10	18

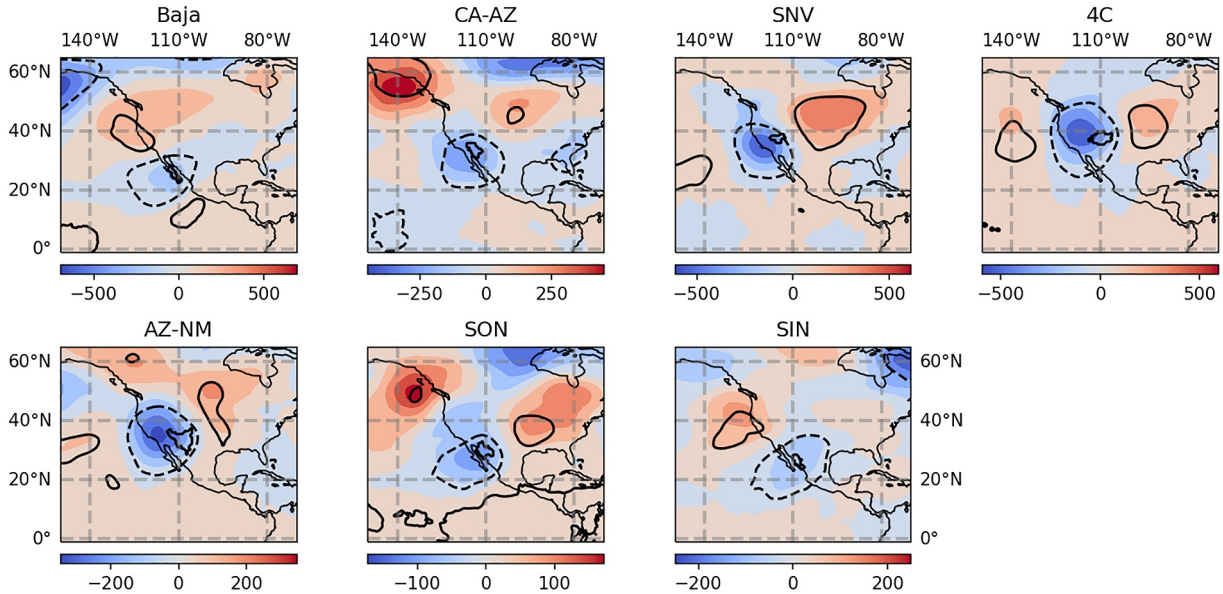

Figure 4. Extreme precipitation event 500 hPa geopotential anomaly composites with units of m^2/s^2. Black contours denote the 95% confidence interval (the solid line denotes positive anomalies and the dashed line denotes negative anomalies). Green outlines delineate subregion domain.

4.3. Relationship Between EPE and Meteorological Features

Since the frontal system record covers 2003 to 2018, and the MCS data set is available from 2001, only TCs, UTTs, GOC surges and mid-tropospheric lows are considered as possible EPE drivers before 2003. Fronts and MCS are included for events from 2003 to 2018. Figure 5 shows the fractions of precipitation amount and EPE events with different drivers before 2003 and after 2003. The events that are not linked with any candidate drivers are denoted as "unclassified" (abbreviated as "Unclass"). Although there are several unclassified events before 2003, the inclusion of frontal systems and MCSs leads to only one unclassified event since 2003. This suggests that the set of features employed in this study essentially covers all EPEs, and that unclassified events before 2003 are likely frontal or MCS events.

It should be noted that the feature classification in Figure 5 is not exclusive (i.e., a UTT event can also be linked with other drivers like GOC surges or MCS). Combined events (i.e., two features simultaneously) are further investigated with EPEs after 2003, since most of the EPEs are associated with two to three drivers. However, there are fewer categories in Baja, CA-AZ and SNV, while the interactions are more complex in SON and SIN.

In most subregions, GOC surges and fronts are the two leading drivers of EPEs, and account for both more relevant events and larger precipitation amounts. TCs have a greater impact on Baja and SON, and MCSs dominate SIN. Mid-tropospheric lows are only somewhat prominent drivers of EPEs over inland subregions (SNV, 4C and AZ-NM), which is consistent with Figure 4 where the geopotential low is more pronounced in these subregions. Figure 5 additionally attribute EPEs over the whole NAM region: considering all subregions together, the precipitation amount and EPE fraction are similarly ranked, with surges being the primary driver with MCSs in second. Despite the fact that only about 20% EPE events are linked to TCs, TCs are associated with almost 40% of EPE precipitation (with overlap with other features), which highlights the substantial precipitation amount that each TC-EPE produces.

For those unclassified events before 2003, we can use our results after 2003 to assess which features were likely missed. Those events from 2003 and after induced by a single driver are shown in Table 3. For SIN it is clear that MCSs are the primary driver of EPEs, with the EPE precipitation solely driven by MCSs exceeding 10%, and about 65% coming from MCSs combined with another feature (Figure 5). This result indicates the importance of MCSs in this area as a driver for EPEs, and explains why this region suffers from a large percentage of "unclassified" events before 2003. Despite MCSs being identified as sole drivers, it's important to acknowledge that large-scale drivers can enable a favorable environment for MCSs. Among the total of 53 MCS events in SIN, only 8 are recognized as occurring without a concurrent large-scale driver, which could be attributed to strict criteria

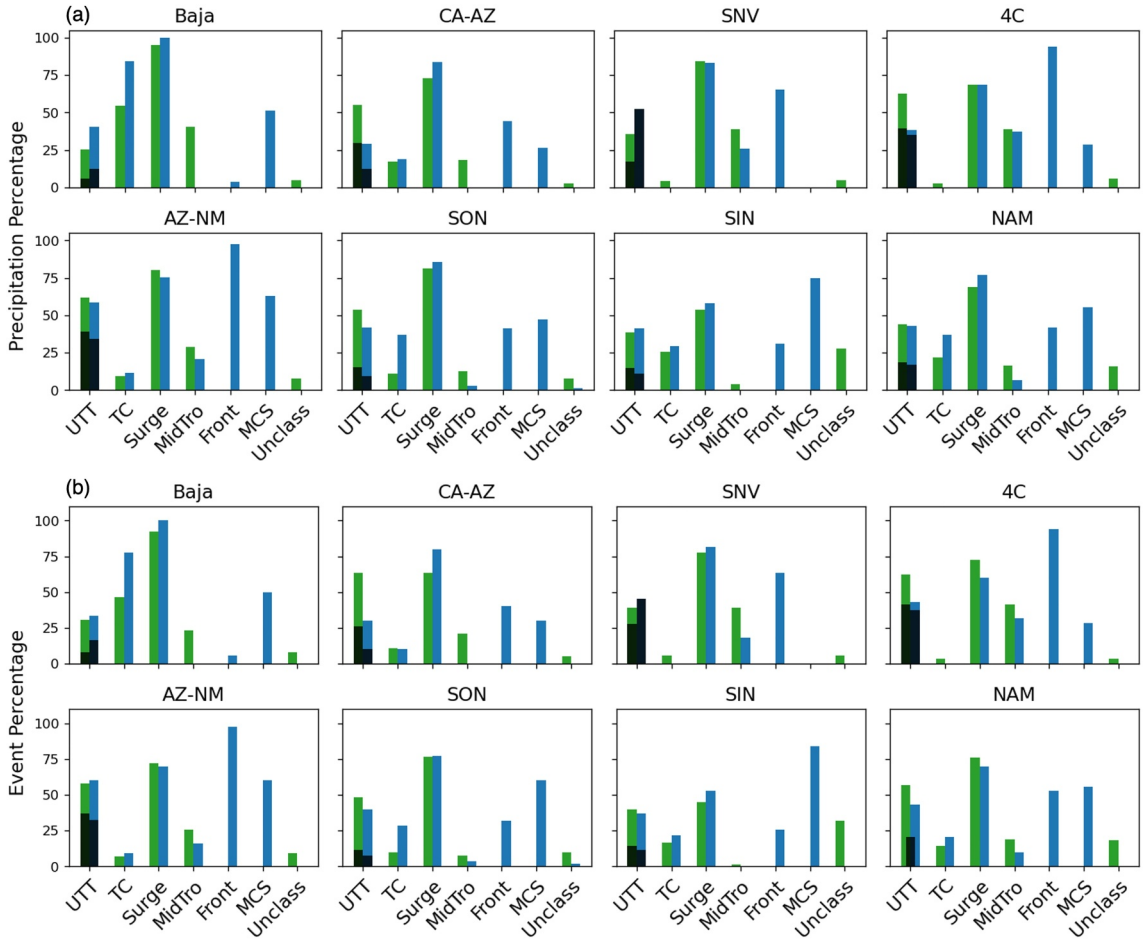

Figure 5. (a) Extreme precipitation event (EPE) precipitation amount percentage (%) and (b) EPE occurrence percentage (%) associated with different feature drivers before 2003 (green) and in or after 2003 (blue). The black color denotes eastward-UTTs. Since a given EPE could be associated with more than one feature, the percentages do not add up to 100%. Fronts and MCSs are not associated with EPEs prior to 2003. "NAM" denotes the whole North American Monsoon region.

that the large-scale conditions do not meet. Future work may be able to employ large-scale conditions as a proxy for these events. Fronts are another feature unavailable in our analysis before 2003, and one that is particularly important over inland subregions (CA-AZ, SNV, and 4C), where the front-only EPE precipitation exceeds 5%. However, mid-tropospheric lows can sometimes be used as a proxy for frontal activity—in fact, all EPEs associated with mid-tropospheric lows after 2003 are also associated with fronts. For SNV, 4C, AZ-NM, and SON, where fronts and mid-tropospheric lows are frequent, the frontal system types are examined against the existence of mid-tropospheric lows. As listed in Table 4, although not all fronts with mid-tropospheric lows are cold fronts, the proportion of cold fronts increases when mid-tropospheric lows are present.

Table 3
Extreme Precipitation Event (EPE) Precipitation Amount (%) Exclusively Associated With a Single Driver After 2003

	CA-AZ	SNV	4C	AZ-NM	SON	SIN
Surge	26.45	19.20	16.54	0	7.44	1.79
UTT	7.93	8.51	0	0	0	0
Front	8.15	8.13	7.50	4.67	0	0
MCS	0	0	0	2.30	3.72	11.43

Note. No EPEs in Baja are exclusively attributed to a single driver, and thus, not included. Tropical cyclones and mid-tropospheric lows, which do not solely contribute to any EPEs, are also excluded.

While essentially all EPEs can be attributed to our six atmospheric drivers, one unclassified event in SON remains after 2003. Further examination of this event's meteorological environment reveals a weak upper-level disturbance (Figure S7 in Supporting Information S1), which likely caused the event's relatively low precipitation rate of 10.9 mm/day (vs. the 95th percentile threshold of 10.7 mm/day).

4.4. Trends in EPE Feature Drivers

As mentioned previously in Section 4.1, both the number of EPEs and EPE precipitation amount have increased in Baja and SON, while EPE

Table 4
Type of Frontal System Present With and Without an Associated Mid-Troposphere Low

	SNV	4C	AZ-NM	SON
Without mid-tropospheric lows				
Cold Fronts	3	6	10	4
Stationary Fronts	2	20	35	15
Fraction of Cold Fronts	0.375	0.231	0.222	0.210
With mid-tropospheric lows				
Cold Fronts	3	8	5	1
Stationary Fronts	0	5	7	1
Fraction of Cold Fronts	1.000	0.615	0.417	0.500

precipitation rate has trended down in CA-AZ. Since we have now classified EPEs by feature type, the trends for each EPE driver in these three subregions are further examined with the same MK test. Because six categories are being tested at the same time, a Bonferroni correction is applied to adjust the confidence level from 0.05 to 0.05/6 ≈ 0.008. The findings are presented in Figure 6, showcasing statistically significant results or outcomes approaching the significant confidence level.

For the number of EPEs in each year, only the trend in TC-related EPEs is significant in SON—there are no significant trends for other categories or regions. Although an upward trend in the number of EPEs is found in Baja, none of the EPE categories have increased significantly, likely due to the strict p-value from Bonferroni adjustment (Perneger, 1998). The likely reason for the increase in EPE count in Baja is the number of TC-EPEs there, which has increased with a p-value of 0.010, a level far more significant than other categories but one that nevertheless does not satisfy our Bonferroni threshold. The trend in precipitation amount is only significant for TC-EPEs in Baja and SON, and there are no significant trends for the remaining categories. Only SON exhibits an increasing trend for TC-EPE precipitation rate, and again the p-value (0.012) for TC-EPE precipitation rate in Baja is the lowest among all the categories, but not significant with the Bonferroni adjustment. This result nonetheless suggests that the significant trends of EPE numbers and total precipitation in Baja and SON are largely explained by an increase in TC-related EPEs and more intense TC rainfall. This, in turn, may be affected by low-frequency variability (Pazos & Mendoza, 2013), or global warming (i.e., observed increases in TC frequency over Baja California (Murakami et al., 2020) and in the eastern North Pacific (Klotzbach et al., 2022)). But it is worth noting that, although the increasing trend is significant in SON, the rate of change is small: the Theil-Sen slope is 0 for TC-induced EPEs and ordinary least squares slope is less than 0.03 EPEs/year. Further careful analysis is necessary to better relate these TC trends with differences in the environment.

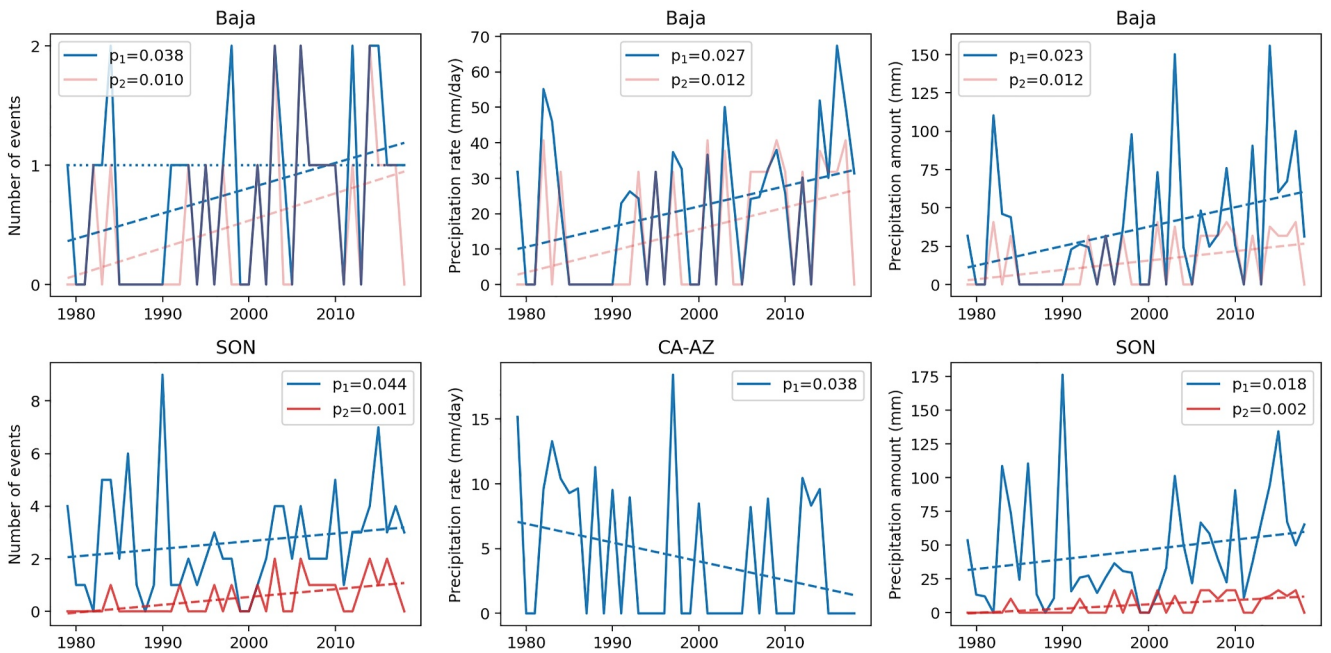

Figure 6. Trend analysis for number of extreme precipitation events (EPEs), and EPE precipitation amount in Baja and SON, and EPE precipitation rate in Baja and CA-AZ. The blue line represents EPEs for the subregion at a significance level denoted by p_1, while the red line depicts EPEs related to tropical cyclone at a significance level indicated by p_2. The fitted ordinary least squares lines are plotted as dashed lines. Only categories nearing the threshold of significance are displayed in the plot. Lines representing non-significant trends are shaded accordingly.

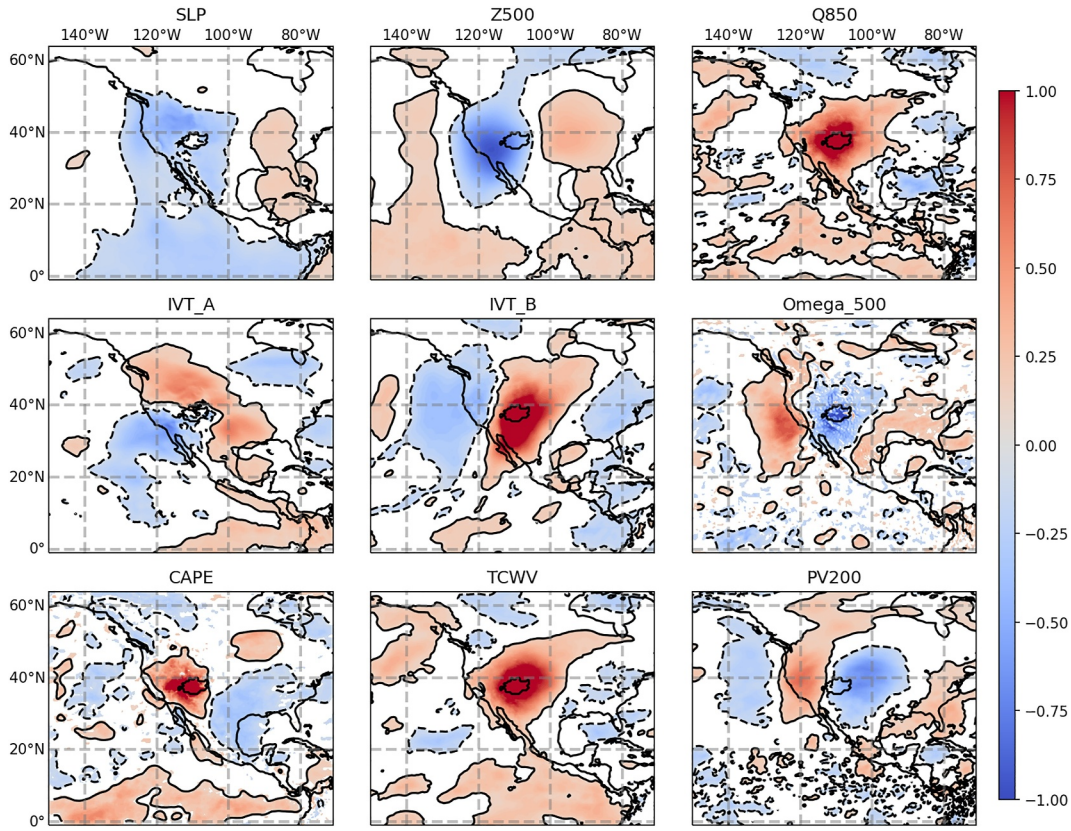

Figure 7. Standardized anomaly composites of extreme precipitation event events in Subregion 4C. Composites are shown at 95% confidence intervals derived from a two-sided *t*-test. Green outlines delineate Subregion 4C.

4.5. EPE Environments

The meteorological field composites for EPEs in each subregion are constructed to reveal the conditions generally present during EPEs. Figure 7 shows the composite for 4C as an example. It is unsurprising that EPEs are coincident with moist conditions: all subregions show local high values of total column water vapor (TCWV) and 850 hPa specific humidity (Q850), mostly associated with strong moisture transport over the GOC channel. Similarly, EPEs occur alongside enhanced vertical uplift, with negative 500 hPa vertical velocity (ω500) anomalies. Positive convective available potential energy anomalies and enhanced moisture also indicate a convectively favorable environment. Figures for other subregions are available in Supporting Information S1 (Figures S8–S13 in Supporting Information S1). Despite common patterns of moisture and uplift, upper-level disturbances are different across subregions: Baja, SON and SIN (coastal areas) show local anomalous negative anomalies in PV200, while a strong gradient of PV200 with positive values to the west and negative values to the east is significant in CA-AZ, SNV, 4C and AZ-NM (inland areas). This difference indicates that UTTs (high PV200 contours) are more influential over SNV, 4C, and AZ-NM, which is consistent with the higher UTT-EPE precipitation fraction over inland areas in Figure 5. Additionally, the local low sea level pressure (SLP) is more pronounced in Baja due to the substantial contribution of TC. There are also differences in the magnitude of the composites across the subregions. Taking TCWV and Φ500 as examples, composite magnitudes are relatively larger for inland areas like SNV and 4C compared with SON and SIN (Figures S14 and S15 in Supporting Information S1). This can be largely attributed to the relative importance of MCSs in SON and SIN (Figure 5) and the weak environmental signature associated with MCSs because of their smaller spatial footprint.

We now turn our attention to composites of environments for different EPE categories. As expected, these composites reveal the meteorological conditions that follow from the feature detection criteria (e.g., anomalous positive PV200 for UTTs) and well-established circulation features (e.g., local low SLP and Φ500 for TCs). Although we have constructed composites for all individual EPE drivers across subregions (figures provided in

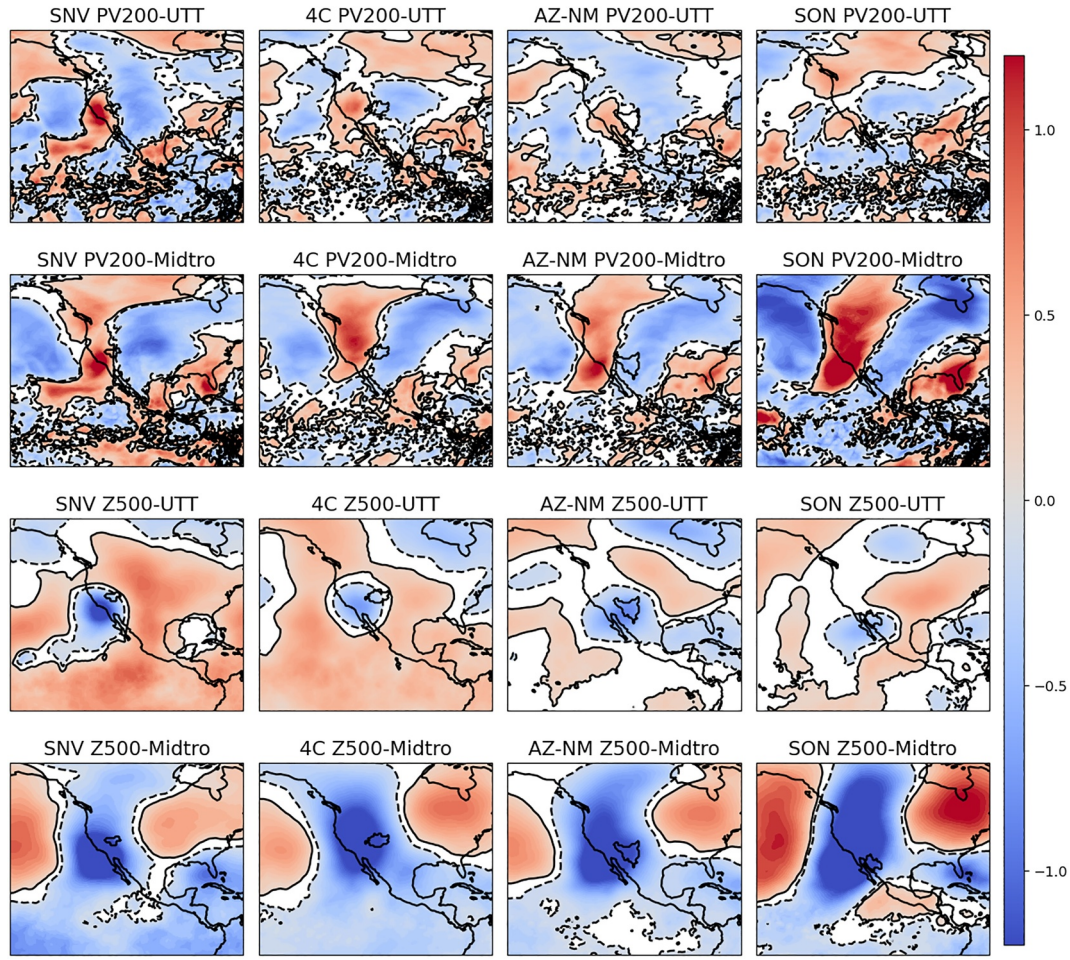

Figure 8. Standardized anomaly composites of UTTs and mid-tropospheric lows for Subregions SNV, 4C, AZ-NM, and SON. Green outlines delineate the Subregions.

Supporting Information S1), instead of exhaustive examination of every singular feature, here we focus on the comparison of UTTs and mid-tropospheric lows, and fronts and mid-tropospheric lows. These particular features share analogous meteorological conditions but exhibit distinctions: mid-tropospheric lows manifest larger horizontal scales than UTTs and exhibit deeper anomalies in comparison to fronts. The composites of GOC moisture surges are also examined, revealing the dominant role of moisture transport perpendicular to GOC for the inland subregions.

4.5.1. UTTs and Mid-Tropospheric Lows

UTTs and mid-tropospheric lows share some common features in PV200 and Φ500, as seen in Figure 8, including anomalously high PV200 and low Φ500. Despite these similarities, the anomalies in Φ500 and PV200 have a larger horizontal scale for mid-tropospheric lows than for UTTs. This is likely related to their horizontal scales: mid-tropospheric lows are likely related to frontal systems and planetary Rossby waves and so have relatively longer wavelengths (Fuentes-Franco et al., 2022); on the other hand, UTT features are shorter waves that largely emerge from RWB events, or tropical disturbances, with an average wavelength around 3,000 km (TUTTs; Chen & Chou, 1994; Kelley & Mock, 1982).

4.5.2. Fronts and Mid-Tropospheric Lows

Fronts and mid-tropospheric lows are more frequent in inland subregions (4C and AZ-NM). As we discussed in Section 4.3 and Table 4, mid-tropospheric lows generally have lower surface temperatures (a consequence of the

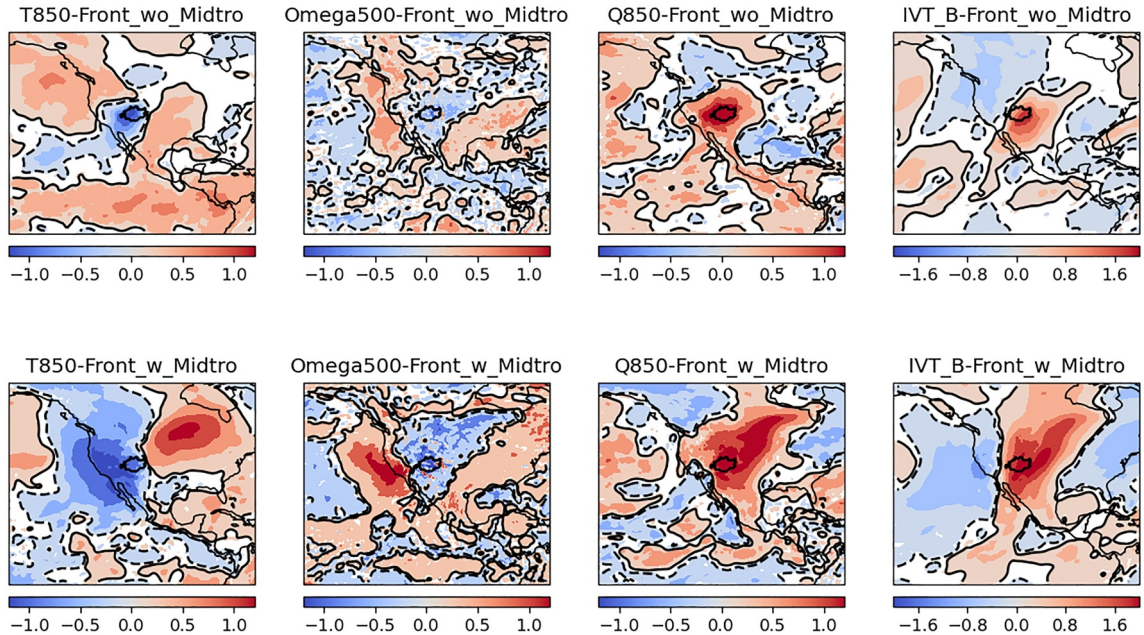

Figure 9. Frontal extreme precipitation event composites in Subregion 4C. The upper row shows fronts without mid-tropospheric lows and the bottom row fronts with mid-tropospheric lows. T850, Omega500, Q850 represent temperature, vertical velocity and specific humidity at 850, 500, and 850 hPa, respectively. IVT-B denotes the integrated vapor transport perpendicular to the Gulf of California channel. The black contours demarcate the 95% confidence interval. Green outline denotes the Subregion 4C.

hypsometric equation), leading to a stronger temperature gradient along the periphery of the low. So it is unsurprising that mid-tropospheric lows and fronts are largely co-occurring and should not be considered entirely independent features. As mentioned earlier in our discussion, mid-tropospheric lows are always associated with fronts for EPEs after 2003. This suggests that features identified as mid-tropospheric lows in our analysis give rise to more intense frontal features. Although both fronts and mid-tropospheric lows can drive uplift, their composites show differences in magnitude and spatial extent: For instance, Figure 9 depicts the composites of frontal EPEs with and without mid-tropospheric lows in 4C. The anomaly magnitudes are observed to be larger for fronts with mid-tropospheric lows. In addition, the spatial extents of moisture and upward motion anomalies are greater when mid-tropospheric lows are co-occurring with fronts. This is certainly related to our geopotential magnitude criterion for mid-tropospheric lows: with $-1{,}000\ m^2/s^2$ as the threshold, the trough is deep enough to be generally associated with anomalously low near-surface temperatures. This cold air enhances the temperature gradient and intensifies frontal systems. In addition, as we discussed in Section 4.5.1, mid-tropospheric lows are also related to planetary waves, which often have longer wavelength, whereas fronts are more localized.

4.5.3. GOC Moisture Surges

Although winds are largely directed along the GOC in the summertime (Bordoni & Stevens, 2006) and IVT-A (the along-gulf vapor transport) is used to derive GOC surges, an enhancement in IVT-B (the gulf-perpendicular transport) is also observed during GOC surge EPEs as shown in Figure 10, with 4C as an example. On the EPE onset dates, the IVT-B anomaly is significant throughout the GOC and 4C, while the IVT-A is depressed over GOC and part of 4C. When examining days prior to EPEs, the positive IVT-A anomalies are apparent over GOC 1 day prior and pronounced 2 days prior. This follows expectations from Figure 2. In contrast to IVT-A, IVT-B anomalies are consistently onshore in the 3-day window and cover a wider range of spatial locations, including both GOC and 4C. The IVT anomalies also exhibit a notable shift in direction over the event: from a flow perpendicular to the GOC to a flow toward the inland regions. These results suggest the important role of onshore moisture transport for EPEs, especially over inland areas (similar composite patterns are observed in AZ-NM, in Supporting Information S1). Additionally, even though the IVT-A is only significant several days prior to the EPE and IVT-A and IVT-B are orthogonal, the geographical position and alignment of the GOC channel make IVT-A representative of onshore moisture transport. A further examination shows the correlations

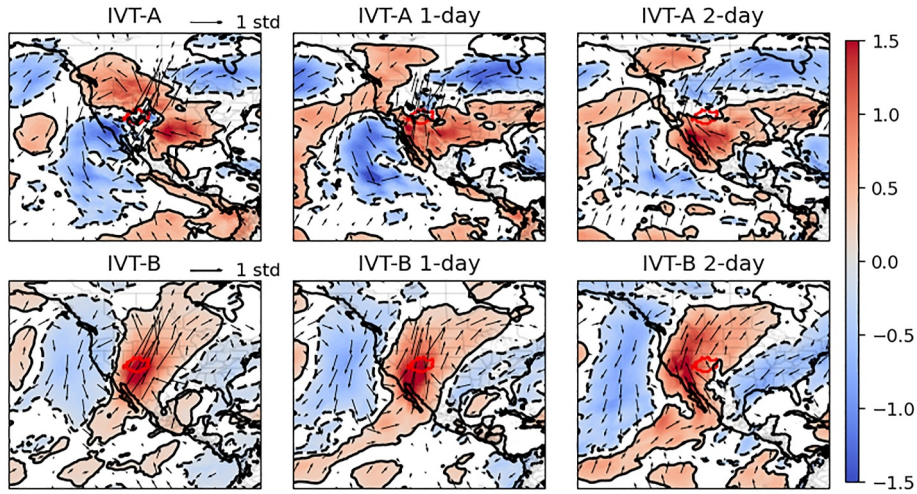

Figure 10. Gulf of California (GOC) moisture surge extreme precipitation event composites of standardized anomalies in Subregion 4C. The left column depicts concurrent composites, middle for 1 day prior and right for 2 days prior, which is also the GOC surge onset date. Black contours show the 95% confidence interval. Vectors represent the integral of vapor flux (IVT) anomalies. Green outline denotes the Subregion 4C.

between IVT-A and IVT-B are significant, although the coefficients are small. Thus, GOC surges identified solely with IVT-A also suggest an enhancement in IVT-B.

4.6. Precipitation Rate Distributions From Atmospheric Features

Although we have shown that essentially all NAM EPEs can be associated with a feature driver, the presence of a feature is, in general, not sufficient to guarantee occurrence of an EPE. To examine precipitation response in the presence of a particular atmospheric feature, we composite the precipitation rate with respect to different drivers and compute the probability of an EPE on rainy days. Previous studies have shown the precipitation rate generally follows a gamma distribution (Martinez-Villalobos & Neelin, 2019; Watterson & Dix, 2003), or a generalized Pareto distribution (GPD), especially for extreme events (Dargahi-Noubary, 1989). While these choices are effective for most of the intensity distribution, the fitted parameters tend to underestimate the probability of extreme precipitation when comparing the cumulative distribution functions to the observed frequency of EPEs under each feature. Consequently, instead of relying on fitted distributions, we use binary EPE frequency and bootstrapping to derive confidence intervals.

The results of this procedure are shown in Figure 11 for single drivers. An analogous figure for double drivers is available in Supporting Information S1 (Figure S16 in Supporting Information S1). Since we defined the threshold for EPEs at the 95th percentile of precipitation, the 5% level in Figure 11 corresponds to the baseline EPE frequency. The single driver with the highest extreme precipitation probability is TCs for CA-AZ, AZ-NM, SON, and SIN, mid-tropospheric lows for Baja and SNV, and MCSs for 4C. Particularly for AZ-NM and SON, presence of a TC suggests EPE probability is five times greater than the baseline. Because the probability of EPE occurrence does not incorporate the frequency of each driver, the single driver with the highest extreme precipitation probability is not the greatest contributor to extreme precipitation shown in Figure 5. For example, in AZ-NM, TCs are the driver with the highest probability of extreme precipitation rates, whereas both the number and precipitation amount of TC-related EPEs are the lowest (Figure 5). This result is consistent with AZ-NM being far from the tracks of nearly all TCs. AZ-NM is also a desert region with a lower threshold for extreme precipitation, compared to coastal areas like Baja, CA-AZ, SON and SIN (Table 1).

Compared with the single drivers, the probability for an EPE to occur when two drivers are present is not necessarily higher than with a single driver (e.g., the probability of an EPE emerging in SON from a combined TC-Midtro (0.20) is less than the probability from a TC alone (0.27)). This suggests two or more features can interact non-linearly, and that precipitation enhancement is not additive. To examine the interactions between candidate drivers, a qualitative assessment is carried out. Since the EPE sample size is limited and the confidence intervals for the EPE frequency are wide, which indicates a large uncertainty, instead of frequencies as single

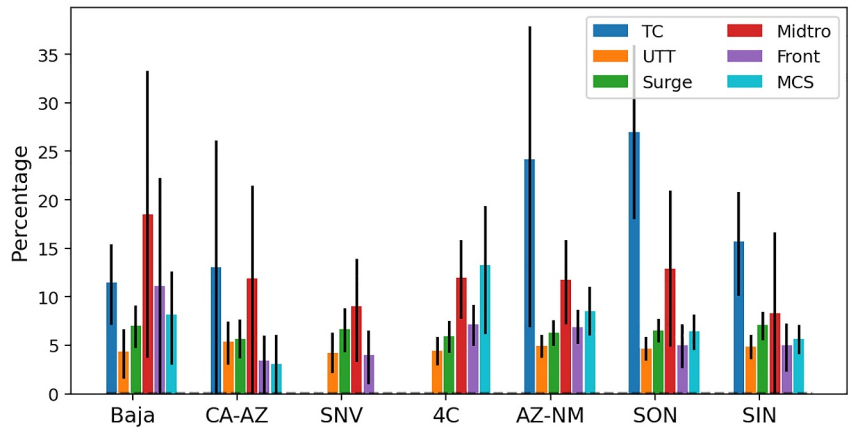

Figure 11. Frequencies of precipitation rates exceeding the extreme threshold, conditioned on the occurrence of single candidate drivers. The error bar shows the 95% confidence interval derived from bootstrap sampling. Probabilities are shown as percentages.

scalars, the GPD probability density function (PDF) is adopted, with a focus on the high precipitation rate regime. Comprehensive results can be found in Supporting Information S1 (Figures S17–S23 in Supporting Information S1). In the following section, we highlight three significant and interesting interactions: a strong association between TCs and GOC surges; amplifying and diminishing effects in the interactions involving mid-tropospheric lows with fronts and TCs with UTTs; and dissimilar interactions with MCSs from westward and eastward UTTs.

4.6.1. TC-Surge Interactions

Given their close association, it is perhaps unsurprising that the TC and TC-Surge PDF curves are similar to each other in both Baja and SIN, as shown in Figure 12. In addition, the number of TC-Surge-related precipitation days (208 for Baja and 160 for SIN) is close to the number of TC-related days (227 for Baja and 178 for SIN), indicative of TCs being closely associated with GOC surges. As Baja and SIN lie toward the south end of the GOC, the precipitation response to TCs and TC-Surges are nearly identical in these regions.

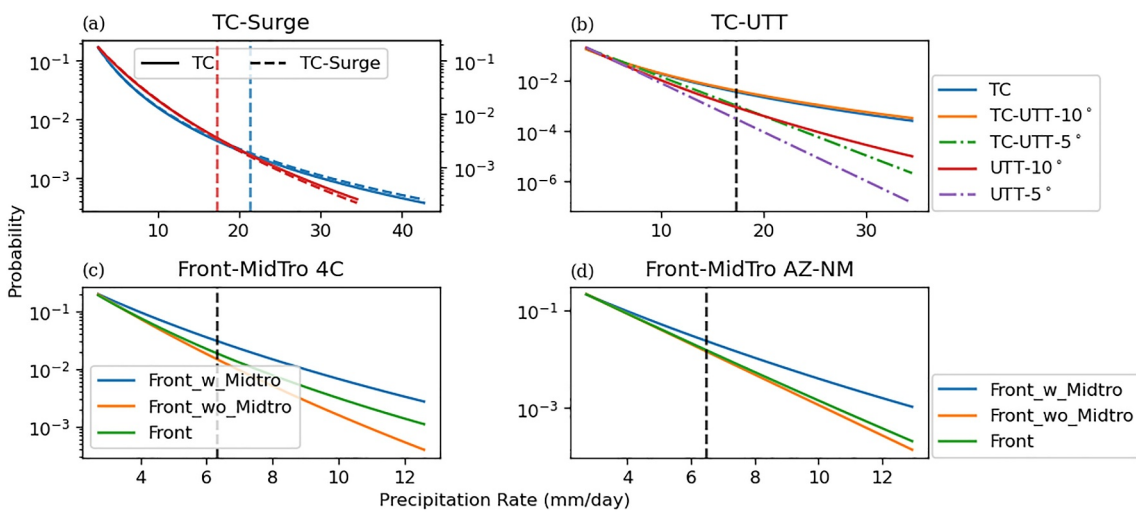

Figure 12. Double-feature generalized Pareto distribution PDF curves with parameters estimated from the extreme precipitation event (EPE) precipitation data set: (a) tropical cyclone (TC) and Gulf of California surge in Baja (blue) and SIN (red); (b) TC and UTT with different distance thresholds in SIN; (c) front and mid-tropospheric lows in 4C and (d) AZ-NM. Dashed vertical lines represent the EPE threshold.

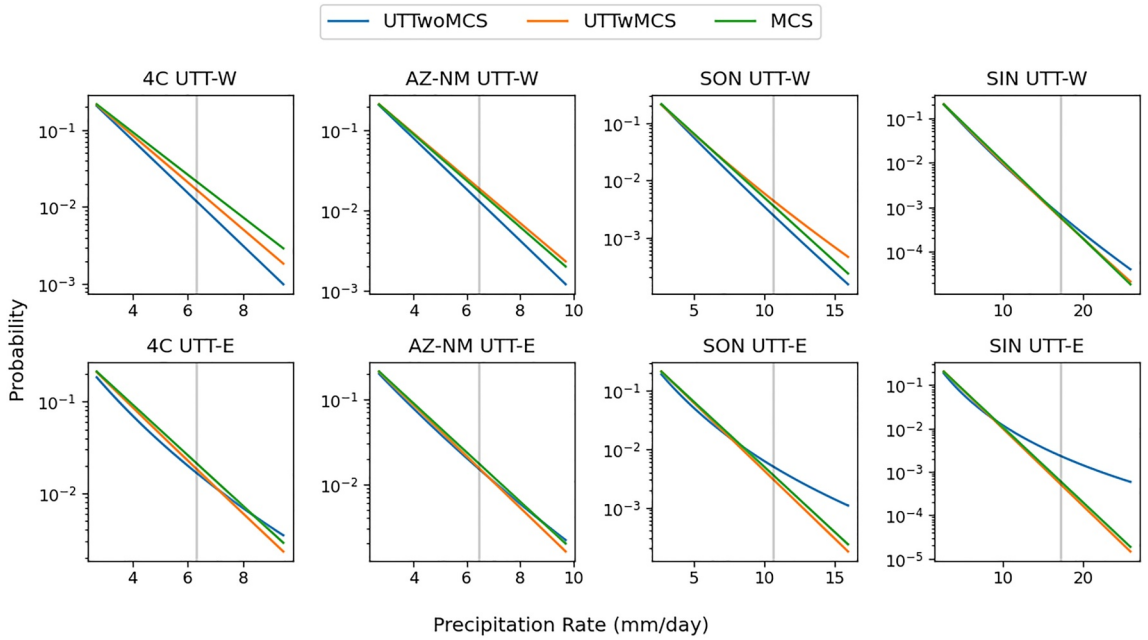

Figure 13. UTT and mesoscale convection system (MCS) precipitation generalized Pareto distribution PDF functions and their interactions in subregions 4C, AZ-NM, SON and SIN. The top row is for westward-UTTs and bottom for eastward-UTTs. UTTwoMCS stands for precipitation induced solely by UTTs, and UTTwMCS represents the precipitation caused by both UTT and MCS.

4.6.2. TC-UTT Interactions

The PDF curves for TC, UTT and TC-UTT precipitation are further compared in SIN since TCs and UTTs are both frequent here. In Figure 12, the TC-UTT-10° (i.e., TC-UTT double driver using the default 10° UTT search radius) precipitation curve is close to the TC curve, while the UTT-10° curve is far below these two curves, indicating much lower probability of high precipitation intensity. The insignificant impact of UTTs on TCs is here attributed to their disparate distance criteria (5° for TCs and 10° for UTTs). TCs are more frequent to the west of SIN while easterly UTTs are dominant (as in Table 2). Since, in a compound event, UTT centers are usually far from the TC centers, the TC precipitation is largely unaffected by UTTs. However, when we decrease the distance criterion to 5° for UTTs, the TC-UTT curve indeed shows lower probabilities for high precipitation rates (Figure 12), indicating that UTTs tend to weaken TC precipitation. A further examination of the composites shows UTTs hinder the eastward moisture transportation by TCs, which decreases the local water content in SIN. This is in accord with previous research showing that UTTs can decrease TC activity (Z. Wang et al., 2020; G. Zhang et al., 2016, 2017).

4.6.3. Fronts and Mid-Tropospheric Lows

Mid-tropospheric lows and fronts are selected as major drivers of EPEs for 4C and AZ-NM since they are frequent in these inland areas. Comparing the precipitation PDFs, fronts are more likely to produce heavy precipitation when mid-tropospheric lows are concurrent for both 4C and AZ-NM as depicted in Figure 12. Examining Figure 9, it's clear that mid-tropospheric lows are associated with larger anomalies in both water content and vertical velocity fields. As in Section 4.3, this suggests that mid-tropospheric lows and strong frontal systems are closely related.

4.6.4. UTTs and MCSs

As shown in Figure 3, eastward-UTTs and westward-UTTs exhibit distinct precipitation anomalies. With this in mind, we consider a decomposition of UTTs by their propagation directions. Figure 13 depicts the UTT-precipitation PDF curves with and without MCSs. For westward UTTs, presence of a MCS will increase the precipitation rate, as the orange curves (UTTwMCS) are always above the blue curves (UTTwoMCS) in the high precipitation rate regimes. To the contrary, precipitation induced by eastward-UTTs tends to be depressed when

Table 5
Dominant Drivers for North American Monsoon and Its Subregions

	Baja	CA-AZ	SNV	4C
EPE precipitation	Surge, TC, MCS	Surge, Front, UTT	Surge, Front, MidTro	Front, Surge, UTT
EPE occurrence	Surge, TC, MCS	Surge Front, MCS/UTT	Surge, Front, UTT	Front, Surge, UTT
	AZ-NM	SON	SIN	NAM
EPE precipitation	Front, Surge, MCS	Surge, MCS, UTT	MCS, Surge, UTT	Surge, MCS, UTT
EPE occurrence	Front, Surge, MCS/UTT	Surge, MCS, UTT	MCS, Surge, UTT	Surge, MCS, Front

Note. First three features are selected. Mesoscale convection system (MCS) and UTT are tied For CA-AZ and AZ-NM.

MCSs are co-occurring, as the UTTwMCS curves are under the UTTwoMCS curves for SON and SIN. This indicates that westward-UTTs enhance precipitation in MCSs by increasing convective activity, as suggested in the case studies in Finch and Johnson (2010) and Newman and Johnson (2012), although the enhancement is small. Additionally, these case studies have also demonstrated that convective systems are more common in the Sierra Madre. This relatively static location for MCS systems is not always at the same distance to the UTT centers during their westward propagation. This mismatch could potentially result in the fragments of precipitation anomaly composites for westward-UTTs observed in Figure 3.

5. Conclusions

This work investigates the meteorological drivers of EPEs in the NAM region from 1979 to 2018. We first delineate the NAM domain and its subregions using the CPC precipitation data set, rather than using political or geographical boundaries. Since this study focuses on precipitation characteristics, we argue that our precipitation-based SOM approach is better suited for the subsequent analysis of precipitation drivers.

Candidate meteorological features investigated as drivers of EPEs include TCs, UTTs, GOC moisture surges, fronts, mid-tropospheric lows and MCSs. This selection appears sufficient to capture all EPE drivers, as essentially all EPEs fall into at least one of these categories, with only one unclassified EPE after 2003. Unsurprisingly, different subregions have different EPE driving features, with most EPEs associated with more than one driver. A comprehensive result is listed in Table 5. Based on the EPE occurrence, GOC surges, MCSs and fronts tend to be the most important features. This finding highlights the utility of developing MCS and front data sets for the NAM region prior to 2003. The attribution of all EPEs to features does not suggest that presence of these drivers is a sufficient condition for EPE occurrence. Indeed, the probability of an EPE given the presence of any individual driver is generally less than 30%. Additionally, the driver with the highest extreme precipitation probability for each subregion is not the driver that produces the most extreme precipitation, reflecting variations in the frequency of each feature driver.

EPE environment composites indicate that EPEs are associated with both high local water vapor content (Q850, TCWV) and upward lifting (ω500). Further examination shows significant positive anomalies of IVT perpendicular to the GOC for inland areas, indicating the important role of onshore moisture transport in addition to IVT along the GOC. Close associations are found between TCs and GOC surges, and between mid-tropospheric lows and fronts. For UTT-EPEs, the propagation direction of the upper-level disturbance plays a major role in the subsequent precipitation anomalies. Because of the direction of the environmental winds, there are more westerly disturbances for northern subregions (e.g., SNV) whereas easterlies are more common for southern subregions (e.g., SON and SIN). Both types of UTTs tend to suppress precipitation to the north of the feature and enhance it to the south, although the enhancement is weak for westward propagating UTTs. Our double driver analysis suggests co-occurring UTTs tend to suppress TC precipitation, but may be enhanced by MCS (although these results are sensitive to subregion).

While our aim is to conduct a comprehensive analysis of NAM EPEs, we acknowledge the limitations imposed by the scope of our study and available computational resources. In addition to the features investigated in this work, there exist several potential drivers to EPEs or the underlying mechanisms driving them, such as tropical easterly waves (Ladwig & Stensrud, 2009) and the Caribbean low level jet (Magaña & Diaz, 2022). Furthermore, sensitivity tests of attribution methods have not been included into the current work. Incorporating such tests in

future studies could provide valuable insights for refining attribution methodologies, considering factors like distance thresholds for UTTs, TCs, and fronts, as well as amplitude thresholds for mid-tropospheric lows. Finally, the methodology developed for NAM region could also extend to other regions to better quantifies the importance of meteorological drivers to EPEs.

Data Availability Statement

ERA5 data can be accessed at https://cds.climate.copernicus.eu (Copernicus Climate Change Service (C3S) Climate Data Store (CDS), 2020). The CPC global precipitation data set is provided by the NOAA PSL, Boulder, Colorado, USA, from their website at https://psl.noaa.gov (Xie et al., 2007). IBTrACS is available from https://www.ncei.noaa.gov/products/international-best-track-archive (Knapp et al., 2018). NWS front data set is available from https://doi.org/10.5281/zenodo.2651361 (Biard, 2019). Our NAM domain shapefiles and GOC moisture surge records can be accessed at Duan et al. (2022).

Acknowledgments
This material is based upon work supported by the U.S. Department of Energy, Office of Science, Office of Biological and Environmental Research, Climate and Environmental Sciences Division, Regional and Global Model Analysis Program, under Awards DE-SC0019367 and DE-SC0016605. Computational resources are from the National Energy Research Scientific Computing Center (NERSC), which is a DOE Office of Science User Facility and the Tempest cluster at UC Davis. Special thanks to Dr. Matthew Igel for helpful discussions.

References

Acero, F. J., García, J. A., & Gallego, M. C. (2011). Peaks-over-threshold study of trends in extreme rainfall over the Iberian Peninsula. *Journal of Climate*, *24*(4), 1089–1105. https://doi.org/10.1175/2010jcli3627.1

Agel, L., Barlow, M., Feldstein, S. B., & Gutowski, W. J. (2018). Identification of large-scale meteorological patterns associated with extreme precipitation in the US Northeast. *Climate Dynamics*, *50*(5–6), 1819–1839. https://doi.org/10.1007/s00382-017-3724-8

Alaya, B., Zwiers, F., & Zhang, X. (2020). An evaluation of block-maximum based estimation of very long return period precipitation extremes with a large ensemble climate simulation. *Journal of Climate*, *33*(16), 6957–6970. https://doi.org/10.1175/jcli-d-19-0011.1

Anagnostopoulou, C., & Tolika, K. (2012). Extreme precipitation in Europe: Statistical threshold selection based on climatological criteria. *Theoretical and Applied Climatology*, *107*(3), 479–489. https://doi.org/10.1007/s00704-011-0487-8

Barlow, M., Gutowski, W. J., Gyakum, J. R., Katz, R. W., Lim, Y.-K., Schumacher, R. S., et al. (2019). North American extreme precipitation events and related large-scale meteorological patterns: A review of statistical methods, dynamics, modeling, and trends. *Climate Dynamics*, *53*(11), 6835–6875. https://doi.org/10.1007/s00382-019-04958-z

Biard, J. C. (2019). National weather service coded surface bulletins, 2003- (netCDF format). *Zenodo*. https://doi.org/10.5281/zenodo.2651361

Biard, J. C., & Kunkel, K. E. (2019). Automated detection of weather fronts using a deep learning neural network. *Advances in Statistical Climatology, Meteorology and Oceanography*, *5*(2), 147–160. https://doi.org/10.5194/ascmo-5-147-2019

Boos, W., & Pascale, S. (2021). Mechanical forcing of the North American monsoon by orography.

Bordoni, S., & Stevens, B. (2006). Principal component analysis of the summertime winds over the Gulf of California: A Gulf Surge Index. *Monthly Weather Review*, *134*(11), 3395–3414. https://doi.org/10.1175/mwr3253.1

Catto, J., Jakob, C., Berry, G., & Nicholls, N. (2012). Relating global precipitation to atmospheric fronts. *Geophysical Research Letters*, *39*(10), L10805. https://doi.org/10.1029/2012gl051736

Cavazos, T., Turrent, C., & Lettenmaier, D. (2008). Extreme precipitation trends associated with tropical cyclones in the core of the North American monsoon. *Geophysical Research Letters*, *35*(21), L21703. https://doi.org/10.1029/2008gl035832

Chen, G. T.-J., & Chou, L.-F. (1994). An investigation of cold vortices in the upper troposphere over the western north pacific during the warm season. *Monthly Weather Review*, *122*(7), 1436–1448. https://doi.org/10.1175/1520-0493(1994)122<1436:aiocvi>2.0.co;2

Cook, B. I., & Seager, R. (2013). The response of the North American monsoon to increased greenhouse gas forcing. *Journal of Geophysical Research: Atmospheres*, *118*(4), 1690–1699. https://doi.org/10.1002/jgrd.50111

Copernicus Climate Change Service (C3S) Climate Data Store (CDS). (2020). The ERA5 global reanalysis. [Dataset]. Retrieved from https://cds.climate.copernicus.eu/

Dargahi-Noubary, G. (1989). On tail estimation: An improved method. *Mathematical Geology*, *21*(8), 829–842. https://doi.org/10.1007/bf00894450

de Carvalho, L. M. V. & Jones, C. (Eds.). (2016). *The monsoons and climate change*. Springer International Publishing. https://doi.org/10.1007/978-3-319-21650-8

Díaz, S., Salinas-Zavala, C., & Hernández-Vázquez, S. (2008). Variability of rainfall from tropical cyclones in northwestern México and its relation to SOI and PDO. *Atmósfera*, *21*(2), 213–223.

Dominguez, C., & Magaña, V. (2018). The role of tropical cyclones in precipitation over the tropical and subtropical North America. *Frontiers in Earth Science*, *6*, 19. https://doi.org/10.3389/feart.2018.00019

Dominguez, F., Miguez-Macho, G., & Hu, H. (2016). WRF with water vapor tracers: A study of moisture sources for the North American monsoon. *Journal of Hydrometeorology*, *17*(7), 1915–1927. https://doi.org/10.1175/jhm-d-15-0221.1

Douglas, A. V., & Englehart, P. J. (2007). A climatological perspective of transient synoptic features during name 2004. *Journal of Climate*, *20*(9), 1947–1954. https://doi.org/10.1175/jcli4095.1

Duan, S., Ullrich, P., & Boos, W. (2022). North American monsoon domain and Gulf of California moisture surges [Dataset]. *Zenodo*. https://doi.org/10.5281/zenodo.8277382

Englehart, P. J., & Douglas, A. V. (2001). The role of eastern north pacific tropical storms in the rainfall climatology of western Mexico. *International Journal of Climatology: A Journal of the Royal Meteorological Society*, *21*(11), 1357–1370. https://doi.org/10.1002/joc.637

Feng, Z., Leung, L. R., Liu, N., Wang, J., Houze Jr, R. A., Li, J., et al. (2021). A global high-resolution mesoscale convective system database using satellite-derived cloud tops, surface precipitation, and tracking. *Journal of Geophysical Research: Atmospheres*, *126*(8), e2020JD034202. https://doi.org/10.1029/2020jd034202

Fettweis, X., Mabille, G., Erpicum, M., Nicolay, S., & den Broeke, M. V. (2011). The 1958–2009 Greenland ice sheet surface melt and the mid-tropospheric atmospheric circulation. *Climate Dynamics*, *36*(1–2), 139–159. https://doi.org/10.1007/s00382-010-0772-8

Finch, Z. O., & Johnson, R. H. (2010). Observational analysis of an upper-level inverted trough during the 2004 North American monsoon experiment. *Monthly Weather Review*, *138*(9), 3540–3555. https://doi.org/10.1175/2010mwr3369.1

Fuentes-Franco, R., Koenigk, T., Docquier, D., Graef, F., & Wyser, K. (2022). Exploring the influence of the north pacific Rossby wave sources on the variability of summer atmospheric circulation and precipitation over the northern hemisphere. *Climate Dynamics*, *59*(7–8), 1–15. https://doi.org/10.1007/s00382-022-06194-4

Geen, R., Bordoni, S., Battisti, D. S., & Hui, K. (2020). Monsoons, ITCZs, and the concept of the global monsoon. *Reviews of Geophysics*, *58*(4), e2020RG000700. https://doi.org/10.1029/2020rg000700

Goswami, B. N., Krishnamurthy, V., & Annmalai, H. (1999). A broad-scale circulation index for the interannual variability of the Indian summer monsoon. *Quarterly Journal of the Royal Meteorological Society*, *125*(554), 611–633. https://doi.org/10.1002/qj.49712555412

Hersbach, H., Bell, B., Berrisford, P., Hirahara, S., Horányi, A., Muñoz-Sabater, J., et al. (2020). The ERA5 global reanalysis. *Quarterly Journal of the Royal Meteorological Society*, *146*(730), 1999–2049. https://doi.org/10.1002/qj.3803

Higgins, R., Yao, Y., & Wang, X. (1997). Influence of the North American monsoon system on the US summer precipitation regime. *Journal of Climate*, *10*(10), 2600–2622. https://doi.org/10.1175/1520-0442(1997)010<2600:iotnam>2.0.co;2

Higgins, W., Ahijevych, D., Amador, J., Barros, A., Berbery, E. H., Caetano, E., et al. (2006). The name 2004 field campaign and modeling strategy. *Bulletin of the American Meteorological Society*, *87*(1), 79–94. https://doi.org/10.1175/bams-87-1-79

Houssos, E., Lolis, C., & Bartzokas, A. (2008). Atmospheric circulation patterns associated with extreme precipitation amounts in Greece. *Advances in Geosciences*, *17*, 5–11. https://doi.org/10.5194/adgeo-17-5-2008

Huang, W., Chen, R., Yang, Z., Wang, B., & Ma, W. (2017). Exploring the combined effects of the arctic oscillation and ENSO on the wintertime climate over East Asia using self-organizing maps. *Journal of Geophysical Research: Atmospheres*, *122*(17), 9107–9129. https://doi.org/10.1002/2017jd026812

Hung, C.-W., & Yanai, M. (2004). Factors contributing to the onset of the Australian summer monsoon. *Quarterly Journal of the Royal Meteorological Society: A Journal of the Atmospheric Sciences, Applied Meteorology and Physical Oceanography*, *130*(597), 739–758. https://doi.org/10.1256/qj.02.191

Igel, M. R., Ullrich, P. A., & Boos, W. R. (2021). Upper-tropospheric troughs and North American monsoon rainfall in a long-term track dataset. *Journal of Geophysical Research: Atmospheres*, *126*(20), e2021JD034541. https://doi.org/10.1029/2021jd034541

Jiang, H., & Zipser, E. J. (2010). Contribution of tropical cyclones to the global precipitation from eight seasons of TRMM data: Regional, seasonal, and interannual variations. *Journal of Climate*, *23*(6), 1526–1543. https://doi.org/10.1175/2009jcli3303.1

Johnson, B. O., & Delworth, T. L. (2023). The role of the Gulf of California in the North American monsoon. *Journal of Climate*, *36*(6), 1541–1559. https://doi.org/10.1175/jcli-d-22-0365.1

Kelley, W. E., & Mock, D. R. (1982). A diagnostic study of upper tropospheric cold lows over the western north pacific. *Monthly Weather Review*, *110*(6), 471–480. https://doi.org/10.1175/1520-0493(1982)110<0471:adsout>2.0.co;2

Klotzbach, P. J., Wood, K. M., Schreck III., C. J., Bowen, S. G., Patricola, C. M., & Bell, M. M. (2022). Trends in global tropical cyclone activity: 1990–2021. *Geophysical Research Letters*, *49*(6), e2021GL095774. https://doi.org/10.1029/2021gl095774

Knapp, K. R., Diamond, H. J., Kossin, J. P., Kruk, M. C., & Schreck, C. J. (2018). *International best track archive for climate stewardship (IBTrACS) project, version 4*. NOAA National Centers for Environmental Information. https://doi.org/10.25921/82TY-9E16

Knapp, K. R., Kruk, M. C., Levinson, D. H., Diamond, H. J., & Neumann, C. J. (2010). The international best track archive for climate stewardship (IBTrACS) unifying tropical cyclone data. *Bulletin of the American Meteorological Society*, *91*(3), 363–376. https://doi.org/10.1175/2009bams2755.1

Kohonen, T., & Honkela, T. (2007). Kohonen network. *Scholarpedia*, *2*(1), 1568. https://doi.org/10.4249/scholarpedia.1568

Kunkel, K. E., Easterling, D. R., Kristovich, D. A., Gleason, B., Stoecker, L., & Smith, R. (2012). Meteorological causes of the secular variations in observed extreme precipitation events for the conterminous United States. *Journal of Hydrometeorology*, *13*(3), 1131–1141. https://doi.org/10.1175/jhm-d-11-0108.1

Ladwig, W. C., & Stensrud, D. J. (2009). Relationship between tropical easterly waves and precipitation during the North American monsoon. *Journal of Climate*, *22*(2), 258–271. https://doi.org/10.1175/2008jcli2241.1

Lee, J.-Y., & Wang, B. (2014). Future change of global monsoon in the CMIP5. *Climate Dynamics*, *42*(1–2), 101–119. https://doi.org/10.1007/s00382-012-1564-0

Liu, F., Chai, J., Wang, B., Liu, J., Zhang, X., & Wang, Z. (2016). Global monsoon precipitation responses to large volcanic eruptions. *Scientific Reports*, *6*(1), 1–11. https://doi.org/10.1038/srep24331

Lund, I. A. (1963). Map-pattern classification by statistical methods. *Journal of Applied Meteorology and Climatology*, *2*(1), 56–65. https://doi.org/10.1175/1520-0450(1963)002<0056:mpcbsm>2.0.co;2

Magaña, V., & Diaz, S. (2022). Inter ocean basin moisture fluxes and the onset of the summer rainy season over southern Mexico. *Frontiers in Climate*, *4*, 1037350. https://doi.org/10.3389/fclim.2022.1037350

Martinez-Villalobos, C., & Neelin, J. D. (2019). Why do precipitation intensities tend to follow gamma distributions? *Journal of the Atmospheric Sciences*, *76*(11), 3611–3631. https://doi.org/10.1175/jas-d-18-0343.1

Mejia, J. F., Douglas, M. W., & Lamb, P. J. (2016). Observational investigation of relationships between moisture surges and mesoscale-to large-scale convection during the North American monsoon. *International Journal of Climatology*, *36*(6), 2555–2569. https://doi.org/10.1002/joc.4512

Mohtadi, M., Prange, M., & Steinke, S. (2016). Palaeoclimatic insights into forcing and response of monsoon rainfall. *Nature*, *533*(7602), 191–199. https://doi.org/10.1038/nature17450

Murakami, H., Delworth, T. L., Cooke, W. F., Zhao, M., Xiang, B., & Hsu, P.-C. (2020). Detected climatic change in global distribution of tropical cyclones. *Proceedings of the National Academy of Sciences*, *117*(20), 10706–10714. https://doi.org/10.1073/pnas.1922500117

Myhre, G., Alterskjær, K., Stjern, C. W., Hodnebrog, Ø., Marelle, L., Samset, B. H., et al. (2019). Frequency of extreme precipitation increases extensively with event rareness under global warming. *Scientific Reports*, *9*(1), 1–10. https://doi.org/10.1038/s41598-019-52277-4

Newman, A., & Johnson, R. H. (2012). Mechanisms for precipitation enhancement in a North American Monsoon upper-tropospheric trough. *Journal of the Atmospheric Sciences*, *69*(6), 1775–1792. https://doi.org/10.1175/jas-d-11-0223.1

Parfitt, R., Czaja, A., & Seo, H. (2017). A simple diagnostic for the detection of atmospheric fronts. *Geophysical Research Letters*, *44*(9), 4351–4358. https://doi.org/10.1002/2017gl073662

Pazos, M., & Mendoza, B. (2013). Landfalling tropical cyclones along the eastern pacific coast between the sixteenth and twentieth centuries. *Journal of Climate*, *26*(12), 4219–4230. https://doi.org/10.1175/jcli-d-11-00411.1

Perneger, T. V. (1998). What's wrong with Bonferroni adjustments. *BMJ*, *316*(7139), 1236–1238. https://doi.org/10.1136/bmj.316.7139.1236

Sierks, M. D., Kalansky, J., Cannon, F., & Ralph, F. (2020). Characteristics, origins, and impacts of summertime extreme precipitation in the Lake Mead Watershed. *Journal of Climate*, *33*(7), 2663–2680. https://doi.org/10.1175/jcli-d-19-0387.1

Stidd, C. (1953). Cube-root-normal precipitation distributions. *Eos, Transactions American Geophysical Union*, *34*(1), 31–35.

Swenson, L. M., & Grotjahn, R. (2019). Using self-organizing maps to identify coherent conus precipitation regions. *Journal of Climate*, *32*(22), 7747–7761. https://doi.org/10.1175/jcli-d-19-0352.1

Turrent, C., & Cavazos, T. (2009). Role of the land-sea thermal contrast in the interannual modulation of the North American monsoon. *Geophysical Research Letters*, *36*(2), L02808. https://doi.org/10.1029/2008gl036299

Ullrich, P. A., Zarzycki, C. M., McClenny, E. E., Pinheiro, M. C., Stansfield, A. M., & Reed, K. A. (2021). TempestExtremes v2. 1: A community framework for feature detection, tracking and analysis in large datasets. *Geoscientific Model Development Discussions*, *14*(8), 1–37. https://doi.org/10.5194/gmd-14-5023-2021

Varuolo-Clarke, A. M., Reed, K. A., & Medeiros, B. (2019). Characterizing the North American monsoon in the community atmosphere model: Sensitivity to resolution and topography. *Journal of Climate*, *32*(23), 8355–8372. https://doi.org/10.1175/jcli-d-18-0567.1

Vera, C., Higgins, W., Amador, J., Ambrizzi, T., Garreaud, R., Gochis, D., et al. (2006). Toward a unified view of the American monsoon systems. *Journal of Climate*, *19*(20), 4977–5000. https://doi.org/10.1175/jcli3896.1

Wang, B., & Fan, Z. (1999). Choice of South Asian summer monsoon indices. *Bulletin of the American Meteorological Society*, *80*(4), 629–638. https://doi.org/10.1175/1520-0477(1999)080<0629:cosasm>2.0.co;2

Wang, B., Li, J., Cane, M. A., Liu, J., Webster, P. J., Xiang, B., et al. (2018). Toward predicting changes in the land monsoon rainfall a decade in advance. *Journal of Climate*, *31*(7), 2699–2714. https://doi.org/10.1175/jcli-d-17-0521.1

Wang, Z., Zhang, G., Dunkerton, T. J., & Jin, F.-F. (2020). Summertime stationary waves integrate tropical and extratropical impacts on tropical cyclone activity. *Proceedings of the National Academy of Sciences*, *117*(37), 22720–22726. https://doi.org/10.1073/pnas.2010547117

Watterson, I., & Dix, M. (2003). Simulated changes due to global warming in daily precipitation means and extremes and their interpretation using the gamma distribution. *Journal of Geophysical Research*, *108*(D13), 4379. https://doi.org/10.1029/2002jd002928

Webster, P. J., & Yang, S. (1992). Monsoon and ENSO: Selectively interactive systems. *Quarterly Journal of the Royal Meteorological Society*, *118*(507), 877–926. https://doi.org/10.1256/smsqj.50704

Wibig, J. (1999). Precipitation in Europe in relation to circulation patterns at the 500 hPa level. *International Journal of Climatology: A Journal of the Royal Meteorological Society*, *19*(3), 253–269. https://doi.org/10.1002/(sici)1097-0088(19990315)19:3<253::aid-joc366>3.0.co;2-0

Xie, P. P., Chen, M., & Shi, W. (2010). CPC unified gauge-based analysis of global daily precipitation. In *Preprints, 24th conf. on Hydrology, Atlanta, GA* (Vol. 2). Amer. Meteor. Soc.

Xie, P. P., Yatagai, A., Chen, M. Y., Hayasaka, T., Fukushima, Y., Liu, C. M., & Yang, S. (2007). CPC unified gauge-based analysis of global daily precipitation. [Dataset]. Retrieved from https://psl.noaa.gov/data/gridded/data.cpc.globalprecip.html

Zhang, G., Wang, Z., Dunkerton, T. J., Peng, M. S., & Magnusdottir, G. (2016). Extratropical impacts on Atlantic tropical cyclone activity. *Journal of the Atmospheric Sciences*, *73*(3), 1401–1418. https://doi.org/10.1175/jas-d-15-0154.1

Zhang, G., Wang, Z., Peng, M. S., & Magnusdottir, G. (2017). Characteristics and impacts of extratropical Rossby wave breaking during the Atlantic hurricane season. *Journal of Climate*, *30*(7), 2363–2379. https://doi.org/10.1175/jcli-d-16-0425.1

Zhang, W., & Zhou, T. (2019). Significant increases in extreme precipitation and the associations with global warming over the global land monsoon regions. *Journal of Climate*, *32*(24), 8465–8488. https://doi.org/10.1175/jcli-d-18-0662.1

Zhuang, Y., Fu, R., & Wang, H. (2020). Large-scale atmospheric circulation patterns associated with US Great Plains warm season droughts revealed by self-organizing maps. *Journal of Geophysical Research: Atmospheres*, *125*(5), e2019JD031460. https://doi.org/10.1029/2019jd031460